

Catalysis Today

ICOSCAR-5 Issue

Manuscript CATTOD-D-15-00586-R1

Numerical study on the wettability dependent interaction of a rising bubble with a periodic open cellular structure

Xuan Cai^{1,2}, Martin Wörner^{1,*}, Holger Marschall³, Olaf Deutschmann^{1,2}

¹Karlsruhe Institute of Technology (KIT), Institute of Catalysis Research and Technology,
Engesserstr. 20, 76131 Karlsruhe, Germany

²Karlsruhe Institute of Technology (KIT), Institute for Chemical Technology and Polymer
Chemistry, Engesserstr. 20, 76131 Karlsruhe, Germany

³Technische Universität Darmstadt, Center of Smart Interfaces, 64287 Darmstadt, Germany

* Corresponding author: Martin Wörner, E-mail: martin.woerner@kit.edu,

Phone +49 721 608 47426, Fax: +49 721 608 44805

Abstract

A phase-field method for interface resolving numerical simulations of two-phase flows with OpenFOAM[®] is validated for the buoyancy-driven rise of a single air bubble through a viscous stagnant liquid using experimental data from literature. The validation encompasses the terminal bubble rise velocity and the instantaneous cutting of the bubble by a solid horizontal cylinder. In the latter process, the numerical method takes into account the equilibrium contact angle of the three-phase system. The numerical method is then used to study the behavior of a single air bubble rising through a representative subdomain of a periodic open cellular structure (POCS) with cubic cell geometry filled with stagnant water. The results indicate that the bubble shape and path do significantly depend on the structure wettability. In the industrial application of POCS for enhancing mass transfer and as catalytic supports, the utilization of structures with high wettability (low contact angles) is expected to be beneficial.

Keywords: Periodic open cellular structure, Wettability, Bubble break-up, CFD simulation, Phase-field method

1 Introduction

Multiphase reactors are found in diverse applications such as in the manufacture of petroleum-based fuels and products, in the production of commodity and specialty chemicals, pharmaceuticals, herbicides and pesticides, polymers and other materials [1]. Among the most popular reactor types are stirred tanks, bubble columns and fixed bed reactors (e.g. trickle beds). Concerning packed beds, structured catalysts and reactors have the ability to outperform randomly packed fixed bed reactors in nearly all aspects [2]. Many industrial bubble columns also require the utilization of internal structures for heat transfer and/or controlling the flow structures and back mixing in the system [3]. The application of structured catalysts and reactor internals allows for partial decoupling of hydrodynamics, transport phenomena and reaction kinetics which opens the way to easier optimization of reactor operations and intensified processes on a large scale [4].

One topic in the German Helmholtz Energy Alliance “Energy Efficient Chemical Multiphase Processes” [5] is the investigation of periodic open cellular structures (POCS) for utilization in bubble column reactors. The POCS elements are produced by additive manufacturing at Friedrich-Alexander-University (FAU) Erlangen-Nürnberg (Germany) via selective electron beam melting which allows precise adjustment to geometric parameters [6-8]. The intention of using POCS as internals in bubble columns is to significantly enhance the gas-liquid mass transfer (by disturbing/renewing the liquid side concentration boundary layer as the rising bubbles interact with the POCS) at only slightly increased pressure drop. In this paper, one fundamental aspect of this process is studied numerically, namely, the rise of a single bubble through a representative subdomain of a POCS. The hydrodynamic interaction between the bubble and the POCS depends on the wettability of the structure. In additive manufacturing processes, it is possible to tune the micro-surface structure to some extent to achieve different equilibrium contact angles. Together with the POCS geometry, patterning its surface wettability (i.e. contact angle) is, therefore, an additional degree of freedom to enhance mass transfer via hydrodynamic interaction between bubbles and structure.

For numerical investigation of the hydrodynamic interaction of a bubble with periodic open cellular structures of different wettability, a phase-field method [9-12] is employed. This method is, in particular, useful in the present context due to its ability of properly describing wetting phenomena [13] and flows with moving contact lines [14, 15]. Recently, a phase-field method was implemented in OpenFOAM® [16] in combination with the Navier-Stokes equations for two-phase flow. The code was validated for fundamental wetting phenomena on a flat homogeneous surface, and for complex wetting processes on a chemically patterned surface [17]. In this paper, the method is further validated for the interaction of a single rising bubble with a horizontal cylinder by comparing numerical results with experimental data from literature. The rise of a single bubble through a tilted periodic open cellular structure is then computed and it is shown that the bubble shape and path depend indeed significantly on the POCS wettability.

The remainder of this paper is organized as follows. In Section 2 the governing equations and the numerical method are described. The code is validated in Section 3. In Section 4 the POCS results are presented and discussed. The paper is closed by conclusions and an outlook in Section 5.

2 Mathematical formulation

2.1 Convective Cahn-Hilliard equation

In the phase-field method, the distribution of the liquid (L) and gas (G) phase is described by an order parameter, C . Here, C takes distinct values $C_L = 1$ and $C_G = -1$ in the bulk phases and varies rapidly but smoothly in a thin transition layer (the diffuse interface). The interface dynamics is governed by the convective Cahn-Hilliard equation

$$\frac{\partial C}{\partial t} + (\mathbf{u} \cdot \nabla) C = \kappa \nabla^2 \phi \quad (1)$$

where t denotes time, \mathbf{u} the velocity field and κ the Cahn-Hilliard mobility. The Cahn-Hilliard chemical potential ϕ consists of a bulk and interface contribution

$$\phi = \frac{\lambda}{\varepsilon^2} C(C^2 - 1) - \lambda \nabla^2 C \quad (2)$$

Here, ε is the capillary width, $\lambda = 3\sigma\varepsilon/2\sqrt{2}$ the mixing energy parameter and σ the interfacial tension [18]. The term on the right-hand-side of Eq. (1) provides a diffusive mechanism for the motion of the contact line at a no-slip wall. Based on the wall free energy formulation at local equilibrium, one can derive the following boundary condition to account for the wettability of the solid substrate [19]

$$\hat{\mathbf{n}}_s \cdot \nabla C = \frac{\sqrt{2} \cos \theta_e}{2} \frac{1 - C^2}{\varepsilon} \quad (3)$$

Here, θ_e is the equilibrium (static) contact angle and $\hat{\mathbf{n}}_s$ is the outward pointing unit normal to the solid surface.

In the non-dimensional form of Eq. (1), two non-dimensional groups appear [19]. The Cahn number $Cn = \varepsilon / L$ relates the capillary width to a macroscopic length scale L while the Peclet number $Pe_C = \sqrt{8/9} LU\varepsilon / \kappa\sigma$ is a measure for the ratio between the advective and diffusive transport of C , where U is a characteristic velocity scale. In this paper, Cn and Pe_C are considered as numerical parameters of the phase-field method, which can be varied via κ and ε . The choice of Cn is influenced, at least, by numerical accuracy, efficiency, and stability [19].

2.2 Navier-Stokes equations

This paper considers two immiscible, incompressible, isothermal Newtonian fluids. Hence, the two-phase flow can be described by the following single-field formulation of the Navier-Stokes equations

$$\nabla \cdot \mathbf{u} = 0 \quad (4)$$

$$\rho_c \left(\frac{\partial \mathbf{u}}{\partial t} + (\mathbf{u} \cdot \nabla) \mathbf{u} \right) = -\nabla p + \nabla \cdot \left[\mu_c (\nabla \mathbf{u} + (\nabla \mathbf{u})^T) \right] + \mathbf{f}_\sigma + \rho_c \mathbf{g} \quad (5)$$

where p is the pressure and \mathbf{g} the gravity vector. For the surface tension term \mathbf{f}_σ , different formulations exist in the literature. Following Jacqmin [9] and Villanueva *et al.* [19], here the relation in Eq. (6) is used

$$\mathbf{f}_\sigma = -C\nabla\phi \quad (6)$$

The density and viscosity fields depend on the order parameter as

$$\rho_C = \frac{1+C}{2}\rho_L + \frac{1-C}{2}\rho_G, \quad \mu_C = \frac{1+C}{2}\mu_L + \frac{1-C}{2}\mu_G \quad (7)$$

where ρ_{UG} and μ_{UG} denote the density and viscosity of the phases. Eqs. (6) and (7) couple the Navier-Stokes Eq. (5) with the Cahn-Hilliard Eq. (1).

2.3 Numerical implementation in OpenFOAM®

The above system of equations is solved numerically using a finite volume method and OpenFOAM®. The open source environment OpenFOAM® is a general library of C++ classes for computational continuum mechanics [20]. Here, version OpenFOAM®-1.6-ext is used. Spatial derivatives are approximated by a high-resolution scheme (Gauss Gamma) and time integration is performed by a second-order two-time-level backward scheme (Gear's method). The time step is chosen such that the maximum Courant number is 0.1. Similar to Ding et al. [10] and Abels et al. [12], a relative density flux due to diffusion of the two-phase components is implemented in the momentum equation to achieve volume conservation for two-phase flows with large density ratios. Further details of the numerical method will be provided in reference [16]. The code has already been verified and validated for several droplet-related test problems [17, 21].

3 Validation for a bubble rising by buoyancy

In this section, the numerical method is validated against recent experimental results of Segers [22] who studied the buoyancy-driven hydrodynamic interaction of a single air bubble rising in a quiescent water-glycerol mixture with a solid horizontal cylinder. The validation proceeds in two steps. First, the influence of mesh resolution, Cahn number, and Peclet number on the bubble rise velocity is studied by 2D axisymmetric simulations and suitable values for these numerical parameters are determined by comparison with the experiment. Second, 3D simulations for the cylinder-induced bubble cutting process are performed and the numerical results are compared with experimental and numerical results from Segers [22].

3.1 Terminal bubble rise velocity

3.1.1 Physical properties and computational set-up

In his experiments, Segers [22] considered glycerin-water mixtures of various compositions in order to vary the Morton number $Mo = (\rho_L - \rho_G)g\mu_L^4 / (\sigma^2\rho_L^3)$ by means of the liquid viscosity. In this section, one specific case is considered where the Morton number is $Mo = 0.064$. The experimental values of the liquid and gas density/viscosity and interfacial tension are $\rho_L = 1237.42 \text{ kg m}^{-3}$, $\rho_G = 1.0 \text{ kg m}^{-3}$, $\mu_L = 0.219 \text{ Pa s}$, $\mu_G = 2 \times 10^{-5} \text{ Pa s}$ and $\sigma = 0.0658 \text{ N m}^{-1}$, respectively. The corresponding liquid-to-gas viscosity ratio is about $\lambda_\mu = \mu_L / \mu_G \approx 10^4$. In the present simulations, $\mu_G = 2.74 \times 10^{-4} \text{ Pa s}$ (which corresponds to $\lambda_\mu = 800$) is used to save computational cost.

All simulations are started from an initially spherical bubble (diameter D , radius $R = D/2$) which is placed in the lower part of the computational domain with both phases being at rest (Fig. 1 a). In the present 2D axisymmetric simulations, the height and width of the computational domain are $H = 8R$ and $W = 6R$, respectively. This domain is discretized by a stationary, structured and uniform grid with mesh size h so that the initial bubble diameter is resolved by $N_D = D/h$ mesh cells. In equilibrium, the variation $-0.9 \leq C \leq 0.9$ occurs over a distance of $L_C = 4.164\varepsilon$ [9]. Taking $L = D$ for the definition of the Cahn number, the corresponding resolution of the interface width is $N_C = L_C / h \approx 4\varepsilon / h = 4Cn N_D$. The boundary conditions for the Navier-Stokes equations are set as *pressureInletOutletVelocity* with zero relative pressure at the top and bottom of the computational domain ($z = 0$, $z = H$) and free slip at $r = W$. For the Cahn-Hilliard equation, zero gradient boundary conditions are used.

As a first test case, one specific experiment from [22] for the bubble diameter $D = 10.3 \text{ mm}$ is considered. This diameter corresponds to an Eötvös number $Eo = (\rho_L - \rho_G)gD^2 / \sigma$ of 19.6. The measured terminal bubble velocity is $U_B = 0.172 \text{ ms}^{-1}$. Fig. 1 shows the computed bubble shape for $Cn = 0.02$, $Pe_C = 1008$ and $N_D = 75$ at four instants in time. Within a traveling distance of about one diameter, the bubble adopts a steady shape and a constant (terminal)

rise velocity, where the driving buoyancy force is in equilibrium with the drag force exerted on the bubble surface by the surrounding liquid. The terminal value of the bubble Reynolds number $Re = \rho_L D U_B / \mu_L$ is 9.85. For the present values of EO , MO and Re , the predicted steady bubble shape agrees well with the established shape regime map in Clift *et al.* [23]. It is also checked that the simulation results of this base case depend neither on W for $W > 5R$ nor on λ_μ for $\lambda_\mu > 800$.

3.1.2 Numerical parameter study

In this section, the effects of three numerical parameters on the bubble rise velocity are studied in order to determine a combination of suitable values. To quantify the effect of mesh resolution, the base case is repeated for three further grids. Fig. 2 shows the time history of the bubble rise velocity for $N_D = 25, 50, 75$ and 100 , respectively. Since $Cn = 0.02$ is kept constant, these values correspond to $N_C = 2, 4, 6$ and 8 , respectively. In Fig. 2 one can observe that the numerical result is independent from N_C when the interface width L_C is resolved by at least six mesh cells.

Sticking to the resolution $N_C = 6$, the influence of the Cahn number is studied next. In Fig. 3, results for $Cn = 0.01$, $Cn = 0.02$ and $Cn = 0.04$ are juxtaposed. The corresponding bubble resolution is $N_D = 150, 75$ and 38 , respectively. As Cn is decreasing, the results for the instantaneous bubble rise velocity are converging. For $Cn \leq 0.02$ the terminal bubble velocity is independent of Cn . In the sequel, only the terminal bubble velocity is of interest. Thus, in all following 2D simulations $Cn = 0.02$ is used to save computational effort.

The last numerical parameter to be varied is the Peclet number. In phase-field methods, Pe_C quantifies a diffusion process that takes place on a length scale which is several orders of magnitude smaller than the bubble diameter and is not of interest here. Thus, Pe_C is treated as a phenomenological parameter here. For the characteristic velocity appearing in the definition of Pe_C , the capillary-viscous velocity scale $U = \sigma / \mu_L$ is used. Following Ding *et al.* [24], $Pe_C = Cn^{-2}$ is set as the first estimate and Pe_C is varied within about one order of

magnitude. The results of the four cases are displayed in Fig. 4 and show a notable variation of the terminal bubble rise velocity. A possible reason for this considerable influence of Pe_c (respectively κ) on the terminal bubble rise velocity is, that in the present simulations the combination of κ and ε does probably not ensure that the results approach the sharp-interface limit. This important topic concerning the phase-field method has not been investigated so far for a freely rising bubble but only in the context of wetting and moving contact lines [18]. Since κ may also be viewed as a material property characteristic of a specific physical system [25, 26], here $Pe_c = 2016$ is chosen since this value produces the best fit with the measured terminal bubble rise velocity of 0.172 ms^{-1} .

3.1.3 Validation

From the results of the previous section, $N_C = 6$, $Cn = 0.02$ and $Pe_c = 2016$ have been identified as suitable numerical parameters for the bubble diameter $D = 10.3 \text{ mm}$ which gave a terminal bubble rise velocity in good agreement with the experiment while allowing at the same time for efficient simulations. Keeping these numerical parameters fixed, four additional simulations are performed for distinct values of the bubble diameter according to the experiment of Segers [22]. The four values for D are 7.4 , 12.4 , 14.2 and 15.7 mm , respectively. The corresponding values of the Eötvös number are 10.2 , 28.3 , 37.3 and 45.6 , respectively. For each diameter the terminal bubble rise velocity is evaluated from the simulation and the corresponding bubble Reynolds number is determined. Fig. 5 shows a comparison of the numerical and experimental values of Re as function of the Eötvös number. For $Eo = 19.5$ the agreement is almost perfect, since for this bubble diameter the experimental terminal bubble velocity was used to determine $Pe_c = 2016$ (cf. Section 3.1.2 and Fig. 4). For $Eo = 10.2$ the computation slightly underestimates the experimental bubble rise velocity, while for the three cases with $Eo > 20$ it is slightly overestimated. These results indicate that the value of Pe_c (or κ), for which the best agreement of the computed terminal bubble rise velocity (and Reynolds number Re) with the measured one is obtained, is a weak

function of the Eötvös number. From Fig. 4 one may expect that the optimal value of Pe_C for obtaining good agreement with the experimental value of Re should slightly increase with the increase of EO . However, no attempts have been undertaken here to quantify this relationship. Overall, the agreement between the computed and experimental terminal bubble rise velocity is, nevertheless, good for a wide range of Eötvös numbers.

3.2 *Cylinder-induced bubble cutting*

3.2.1 *Computational set-up*

Reproducing the cutting of a rising bubble by a solid horizontal cylinder requires 3D simulations. Here, one quarter of the problem is considered with two symmetry-planes. The computational domain is a cuboid with cross-section $4R \times 4R$ and height $12R$. In the upper part of the domain, one half of a horizontal cylinder with diameter D_{cyl} is positioned. The initially spherical bubble is released at a distance sufficiently below the cylinder so that the bubble has obtained its terminal shape and velocity when it hits the cylinder. At the cylinder surface, no-slip boundary conditions are used for the velocity field in combination with a prescribed equilibrium contact angle boundary condition for the order parameter, cf. Eq. (3). The boundary conditions at the top and bottom as well as at the outer lateral faces of the computational domain are the same as in Section 3.1.1. The same holds for the physical properties of both phases. The values for the bubble diameter $D = 9.14 \text{ mm}$ and the cylinder diameter $D_{cyl} = 3.1 \text{ mm}$ are chosen in accordance to the experiment [22].

3.2.2 *Mesh resolution study*

For numerical simulation of a bubble interacting with a solid structure, Cn and N_C are critical parameters of the phase-field method. Both decide on the degree of details one could obtain for phenomena at the local gas-liquid-solid contact region. As Cn is diminishing, local features can be captured more accurately. On the other hand, decreasing Cn may lead to a drastic increase of computational cost, given that N_C mesh cells are necessary for resolving

the diffuse interface while the total number of mesh cells scales as $(N_c / Cn)^3$ in 3D simulations. The focus of the present study is the validation of the method concerning the global bubble shape and the bubble break-up behavior. Hence, $Cn = 0.04$ is chosen for all 3D simulations. This rather large value is justified here since the results from Section 3.1 suggest that the terminal bubble velocity is not significantly affected by this choice. The value of the Peclet number is set to $Pe_c = 1000$.

For the above combination of Cn and Pe_c , three simulations are performed where the mesh resolution is varied according to $N_c = 2, 4$ and 6 . Fig. 6 compares the time evolution of the gas-liquid interfacial area (A_i) for the three resolutions. Here, A_i is evaluated as the area of the surface within the computational domain where C is zero. Note that in Fig. 6 time $t = 0$ does not correspond to the release time of the spherical bubble, but to the time when the bubble has adopted its terminal shape and terminal velocity and has reached a certain position below the cylinder. Fig. 6 shows that as the bubble approaches the cylinder, the interfacial area increases (due to bubble deformation) until $t \approx 0.15$ s. At this moment, the bubble breaks up into two daughter bubbles and the interfacial area decreases in time. Fig. 6 shows that $N_c = 4$ is a good compromise between accuracy and computational effort so that this values will be used in the following simulations in combination with $Cn = 0.04$ and $Pe_c = 1000$.

3.2.3 Validation

The present phase-field method requires the input of the equilibrium contact angle θ_e to account for the surface wettability by Eq. (3). Unfortunately, in the thesis of Segers [22] no information about θ_e is given. According to personal information, the cylinder was made of stainless steel. Wang *et al.* [27] measured the contact angle of stainless steel for air and three different liquids and found that θ_e is in the range of $32^\circ - 54^\circ$. In this subsection, results for $\theta_e = 60^\circ$ are presented and the influence of the contact angle is studied in the next subsection.

Fig. 7 shows a comparison of the present phase-field simulation results for the bubble cutting process with the experiments of Segers [22]. Also shown are numerical results of Segers [22] which are obtained by a hybrid immersed-boundary volume-of-fluid (IBM-VOF) method described by Baltussen [28]. The time $t = 0$ is chosen so that the position of the bubble below the cylinder is about the same in Fig. 7 a), f) and k). For this instant in time, the numerical simulations with both methods have already achieved an equilibrium bubble shape (Fig. 7 f and k) which is comparable to that in the experiment (Fig. 7 a). When the distance between the bubble and the cylinder is smaller than a few millimeters, the bubble front flattens (Fig. 7 b, g and l). As the bubble further approaches the cylinder, the bubble deformation increases and a thin liquid film forms below the cylinder (Fig. 7 c, h and m). The thickness of this film decreases in time until two daughter bubbles develop which are connected by a thin gas filament (Fig. 7 d, i and n). After the breakup process, both daughter bubbles are detached from the cylinder and rise separately (Fig. 7 e, j and o).

Overall, the present phase-field simulation results agree very well with the experiments and numerical simulations in Segers [22]. However, the duration of the entire cylinder-induced bubble cutting process in the present simulations is slightly longer. The reason is that the terminal bubble velocity is slightly under-predicted when using $C_n = 0.04$ and $N_c = 4$, as implicated by Fig. 2 and Fig. 3. Due to the rather large value for C_n and the rather low value for N_c the gas filament below the cylinder is notably thicker as compared to the experiment (Fig. 7 d and n). In the thesis of Segers [22] it is reported that in the experiment some very tiny gas pockets forming from the gas filament are observed at the bottom of the cylinder after the mother bubble break-up (not shown in the current experimental image). Capturing these satellite bubbles on such a small scale is not possible with the present mesh resolution. Though such a satellite bubble is observed in the IBM-VOF results (Fig. 7 j), Segers [22] points out that the shape and dynamics of such small bubbles cannot be resolved properly in his simulation, due to the limitation of mesh resolution.

3.2.4 Influence of cylinder wettability

To study the influence of the cylinder wettability, two additional simulations have been performed for $\theta = 30^\circ$ and 90° keeping all other parameters fixed. Fig. 8 shows the interface evolution for the contact angles 30° , 60° and 90° . Note that the instants in time differ from those in Fig. 7 in order to highlight the influence of θ_c more clearly. Until $t = 0.11\text{ s}$ the bubble deformation is not influenced by the cylinder wettability (Fig. 8 a, f and k). Differences arise at $t = 0.15\text{ s}$. For $\theta_c = 30^\circ$, the gas is not in direct contact with the cylinder (Fig. 8 b) whereas such a contact exists for $\theta_c = 90^\circ$ (Fig. 8 l). This is attributed to the hydrophilicity, which is larger for $\theta_c = 30^\circ$ so that the liquid has a higher tendency to get in contact with the cylinder. This feature also contributes to the differences observed for $t = 0.19\text{ s}$, where two daughter bubbles have formed (Fig. 8 c, h and m). Comparing the cases $\theta_c = 30^\circ$ and $\theta_c = 60^\circ$, the two daughter bubbles show roughly the same shape once they get detached from the cylinder (Fig. 8 d and i) and during their further rise (Fig. 8 e and j). In contrast, the daughter bubbles for $\theta_c = 90^\circ$ exhibit a distinct evolution. Due to the larger adhesion forces, the gas stays longer in contact with the cylinder as compared to the more hydrophilic cases. Instead of escaping separately, as in the simulations for $\theta_c = 30^\circ$ and $\theta_c = 60^\circ$, the lower ends of the two daughter bubbles stay always in contact with the cylinder for $\theta_c = 90^\circ$. In the latter case, the contact lines slide to the upper end of the cylinder (Fig. 8 m) where they meet and reconnect (Fig. 8 n) to a single bubble. For $t = 0.26\text{ s}$, the re-coalesced bubble (Fig. 8 o) is not axi-symmetric; a detailed inspection of the bubble shape (not shown here) indicates that its horizontal dimension perpendicular to the cylinder axis is much larger than its horizontal dimension along the cylinder axis. One may expect that the bubble relaxes to an axisymmetric shape during its further rise. However, this process is not simulated here, because it requires a higher computational domain.

Fig. 9 shows the influence of θ_c on the time evolution of the gas-liquid interfacial area during the bubble-cutting process. Two features are worth noting. First, the largest value of A_1 occurs for $\theta_c = 30^\circ$, i.e. the lowest contact angle. Second, the peak values of A_1 mark the

instant in time when the bubble break-up occurs (cf. Section 3.2.2). Thus, the bubble split occurs earliest for $\theta_e = 90^\circ$ and latest for $\theta_e = 30^\circ$. Both features have their origin in the increasing hydrophilicity and, accordingly, the weakening tendency of the solid to attract gas when θ_e is declining, as discussed previously.

4 Bubble rise through a periodic open cellular structure

In this section, the wettability dependent interaction of a bubble rising in a periodic open cellular structure with cubic cell geometry is studied. At the present stage, the numerical results are predictions since no experimental data for this process are available in the literature which could be used for comparison and validation.

4.1 Fluid properties and computational set-up

Due to the particular practical relevance, now an air-water system is considered. The values of the density, viscosity and interfacial tension are as follows: $\rho_L = 998 \text{ kg m}^{-3}$, $\rho_G = 1.205 \text{ kg m}^{-3}$, $\mu_L = 8.9 \times 10^{-4} \text{ Pa s}$, $\mu_G = 1.81 \times 10^{-5} \text{ Pa s}$ and $\sigma = 0.072 \text{ N m}^{-1}$. This corresponds to a Morton number $Mo = 1.65 \times 10^{-11}$. The geometry and characteristic dimensions of the POCS with cubic cell structure are given in Fig. 10 as provided by FAU Erlangen-Nürnberg. The entire structure is tilted around the horizontal axis by an angle of 45° . The figure shows the computational domain used in the present simulations, which is a representative subdomain of a real POCS. All cases start from fluids at rest with a spherical bubble ($D = 4 \text{ mm}$, $Eu = 2.2$) placed in the lower part of the computational domain (Fig. 11 a, b and c). To make the numerical study more general, the centroid of the bubble is slightly shifted leftward from the symmetry plane, since a perfect symmetrical spatial alignment occurs infrequently in real scenarios. The boundary conditions are the same as described in the previous section. The fluid domain is meshed by a uniform and stationary grid where the bubble diameter is resolved by $N_D = 25$ mesh cells. The simulations are performed with $Cn = 0.04$ and $Pe_C = 1000$.

4.2 Results

To study the effect of structure wettability, five simulations are performed where the equilibrium contact angle is varied in steps of 30° within the range $0^\circ \leq \theta_c \leq 120^\circ$. Fig. 11 shows the results for $\theta_c = 0^\circ$, 90° and 120° in a 3D perspective view for six different instants in time. Driven by the buoyancy force, the bubble rises and reaches the horizontal strut above within a short time. Due to the difference in surface wettability, very distinct bubble-strut interaction behaviors are observed, e.g. at $t = 0.045s$. For $\theta_c = 0^\circ$, the bubble deforms to a concave shape to minimize direct contact with the solid structure (Fig. 11 d), while in the case $\theta_c = 90^\circ$ one finds not only an increased connection area with the horizontal strut, but the bubble also gets into contact with the two lateral struts (Fig. 11 e) due to a strengthened tendency of the solid phase to attract the gas phase. This aerophilic effect of the solid surface is further augmented for $\theta_c = 120^\circ$ where the bubble enwraps the horizontal strut (Fig. 11 f). For both contact angles $\theta_c = 0^\circ$ and 90° , the bubble continues its rise after the contact with the first horizontal strut, yet in a different manner. In the case $\theta_c = 0^\circ$, the bubble is moving upwards in a “detached” mode from the solid structure, either with close-to-spherical shape in the middle of the cell window (Fig. 11 g) or deformed into a cashew-like shape when it approaches the second and third horizontal strut (Fig. 11 j and p). For $\theta_c = 90^\circ$, the mode is switched to “attached” as the bubble adheres to the solid structure during its entire rise as it is virtually “climbing-up” the cell structure. For instants in time when its centroid is close to the center of a cell window (Fig. 11 k and n), the bubble shape is similar to an ellipsoid that is in direct contact with the four surrounding struts. Compared to these two cases, the bubble behavior for $\theta_c = 120^\circ$ is completely different. Under such hydrophobic conditions, the adhesion force exerted by the solid structure on the bubble is strong enough to completely counteract the buoyancy force that lifts the bubble up. Hence, the bubble ceases to rise and is captured in the lower part of the cubic cell (Fig. 11 l, o and r).

In Fig. 12, a 2D side view is shown to facilitate the analysis and comparison. In addition to the cases $\theta_c = 0^\circ$ and 90° discussed above, results for $\theta_c = 60^\circ$ are added. The instants in

time are the same as in Fig. 11. The results for the time $t = 0.045\text{s}$ (when the bubble interacts with the first horizontal strut) show that the bubble concavity increases as θ_c is reduced from 90° to 0° (Fig. 12 f, e and d). At later instants in time, only the case with $\theta_c = 0^\circ$ exhibits such cashew-like bubble shapes each time the bubble approaches a horizontal strut (Fig. 12 j and p). In contrast, such highly concave bubble shapes do not occur in the further course of the simulation cases with $\theta_c = 60^\circ$ and 90° . For the latter two contact angles, the gas is frequently in direct contact with the solid, a feature that is not observed for $\theta_c = 0^\circ$. For the simulation with $\theta_c = 30^\circ$ the results are not shown due to space limitations and because they are in general similar to those for $\theta_c = 0^\circ$.

4.3 Discussion

The results from the previous section show that the bubble shape and path do significantly depend on the equilibrium contact angle. In this section, the implications of the above results for practical applications are discussed.

The results for $\theta_c = 120^\circ$ indicate that hydrophobic POCS are unsuited as bubble column internals in industrial practice as they show a tendency for wettability-induced bubble capture and immobilization. The latter may lead to agglomerates of captured bubbles which might coalesce and form larger bubbles, a phenomenon which should be prevented for two reasons. First, due to the vanishing relative velocity between the phases and the reduced volume-specific gas-liquid interfacial area, the mass transfer rate is decreased. Second, many bubble column reactor applications contain oxygen in the gas phase. Large accumulations of oxygen may give rise to explosive conditions and thus pose a potential safety hazard in chemical plants.

In the simulation with $\theta_c = 90^\circ$, the bubble is always in contact with the solid surface as it is climbing up the POCS but the bubble is not immobilized. However, the temporal trapping of the bubble by the four struts forming a cell window may also lead to unwanted coalescence

between bubbles that climb up in laterally neighboring cells. Thus, also POCS with a contact angle of about 90° appear to be unsuited.

The differences between the simulations for $\theta_c = 60^\circ$, 30° and 0° are less pronounced than those between 60° and 90° and between 90° and 120° , respectively. Nevertheless, several effects can be noted as the contact angle decreases from 60° to 0° . First, during each interaction with a horizontal strut the bubble deformation (concavity) increases. During such a deformation, the liquid side concentration boundary layer is disturbed. As a consequence, liquid with lower concentration reaches the interface which increases the driving concentration gradient and thus the gas-liquid mass transfer. Second, the results for $\theta_c = 0^\circ$ show that during its rise the bubble is alternatingly accelerated (in the cell center, by buoyancy) and decelerated (by horizontal struts), which may further enhance mass transfer. After the interaction with the strut at $t = 0.175s$ (Fig. 12 p), the bubble even bounces back (not shown here) due to an almost head-on collision. Such a bounce-back is not observed for the case with $\theta_c = 60^\circ$, where the bubble rises along an almost rectilinear path for $t \geq 0.075s$. For $\theta_c = 0^\circ$ in contrast, the bubble rises on a zigzag-like pathway as it changes its previous course after each interaction with a horizontal strut. Such a trajectory implicates a lower effective vertical rise velocity and thus a longer residence time of the bubble as compared to the case for $\theta_c = 60^\circ$.

Overall, the present numerical study provides a clear evidence that tuning the wettability to hydrophilic conditions (i.e. to low values of θ_c) can promote mass transfer. Such hydrophilic conditions are also potentially beneficial for applications in heterogeneous catalysis where the POCS act as a catalytic support. The present results indicate that for sufficiently hydrophilic conditions ($\theta_c \leq 30^\circ$) there exists always a thin liquid film between the gas bubble and the solid struts which provides (especially for the horizontal struts) a very short diffusion path for gaseous educts from the gas bubble through the liquid film to the active catalytic sites.

5 Summary and outlook

In this paper, a finite-volume based phase-field method implemented in OpenFOAM® is validated by comparing numerical results for the rise of a single bubble through a viscous liquid and the bubble cutting by a horizontal cylinder with recent experimental data from literature. The code is used to study the influence of the cylinder wettability on the instantaneous cutting process by variation of the equilibrium contact angle θ_e , which serves as an input parameter in the numerical method. The numerical results indicate a notable influence of the contact angle. For $\theta_e \leq 60^\circ$, the bubble breaks up into two daughter bubbles which rise separately, whereas the daughter bubbles reconnect to a single bubble for $\theta_e = 90^\circ$.

The method is used to numerically study the rise of a single air bubble through a water filled periodic open cellular structure (POCS) as they are promoted and manufactured at FAU Erlangen-Nürnberg by additive manufacturing. Five different contact angles in the range $0^\circ \leq \theta_e \leq 120^\circ$ are investigated. While at the present stage, the numerical results are predictive in nature, they are physically sound and there is clear evidence that bubble hydrodynamics is significantly influenced by the POCS wettability. For enhancing mass transfer and as catalytic support, POCS with high wettability (low contact angle) appear to be advantageous according to the present findings. In additive manufacturing, the wettability can be tuned to some extent. In addition to the POCS geometry, patterning the wettability of the structure surface is thus an additional suitable parameter to enhance mass transfer and catalytic reactions via hydrodynamic interaction between bubbles and structure.

The present work is pioneering and opens the field for several follow-up studies with a different focus. First of all, detailed experimental studies on the cylinder-induced bubble cutting process for different wettability conditions are missing in the literature, but would be highly valuable for further validation of the present phase-field method as well as other interface-resolving numerical methods. Detailed experimental studies on the rise behavior of single (and multiple) bubbles through periodic open cellular structures with different wettability

would also be highly welcome in order to confirm the present numerical findings. Once further validated by such experimental data, the present method can be used to explore the behavior of single bubbles in POCS of different wettability by studying e.g. the effect of the ratio between bubble size and cell window size for cubic cell geometries, or the interaction between multiple bubbles.

Acknowledgement

This work is funded by the Helmholtz Energy Alliance “Energy-efficient chemical multiphase processes” (HA-E-0004). We thank our project partners from FAU Erlangen-Nürnberg (Prof. W. Schwieger, Prof. H. Freund) and TU Hamburg-Harburg (Prof. M. Schlüter, C.O. Möller) for providing the POCS geometry via a stl file. X.C also thanks Prof. P.T. Yue (Virginia Tech) for stimulating discussions. Some of the numerical results in this work are obtained using computational resources of bwHPC (<http://www.bwhpc-c5.de/index.php>), funded by the Ministry for Education and Research (BMBF) and the Ministry for Science, Research and Arts Baden-Wuerttemberg (MWK-BW). We also acknowledge the support of the bwHPC-c5 tiger team.

Nomenclature

A_i	[m ²]	gas-liquid interfacial area
C	[-]	order parameter
Cn	[-]	Cahn number
d_s	[m]	strut diameter
D	[m]	bubble diameter
D_{cyl}	[m]	diameter of solid cylinder
Eo	[-]	Eötvös number
\mathbf{g}	[m s ⁻²]	gravity vector
g	[m s ⁻²]	gravitational acceleration
h	[m]	mesh size

H	[m]	height of computational domain
L	[m]	macroscopic length scale
L_C	[m]	interface width
Mo	[-]	Morton number
$\hat{\mathbf{n}}_s$	[-]	unit normal vector to the solid surface
N_C	[-]	number of mesh cells per interface width
N_D	[-]	number of mesh cells per bubble diameter
p	[N m ⁻²]	pressure
Pe_C	[-]	Peclet number in Cahn-Hilliard equation
r	[m]	radial coordinate
R	[m]	bubble radius
Re	[-]	bubble Reynolds number
s	[m]	window size of cubic cell
t	[s]	time
U	[m s ⁻¹]	characteristic velocity scale
\mathbf{u}	[m s ⁻¹]	velocity field
W	[m]	width of computational domain
z	[m]	vertical coordinate

Greek symbols

ε	[m]	capillary width
κ	[m ³ s kg ⁻¹]	mobility
λ	[J m ⁻¹]	mixing energy parameter
λ_μ	[-]	liquid-to-gas viscosity ratio
μ	[Pa s]	dynamic viscosity
ϕ	[J m ⁻³]	Cahn-Hilliard chemical potential
ρ	[kg m ⁻³]	density
θ_e	[°]	equilibrium contact angle

Subscripts

G	gas phase
L	liquid phase

References

- [1] M.P. Dudukovic, F. Larachi, P.L. Mills, Multiphase reactors - revisited, *Chem Eng Sci*, 54 (1999) 1975-1995.
- [2] K. Pangarkar, T.J. Schildhauer, J.R. van Ommen, J. Nijenhuis, F. Kapteijn, J.A. Moulijn, Structured packings for multiphase catalytic reactors, *Ind Eng Chem Res*, 47 (2008) 3720-3751.
- [3] A.A. Youssef, M.H. Al-Dahhan, M.P. Dudukovic, Bubble Columns with Internals: A Review, *Int J Chem React Eng*, 11 (2013).
- [4] J. Gascon, J.R. van Ommen, J.A. Moulijn, F. Kapteijn, Structuring catalyst and reactor - an inviting avenue to process intensification, *Catal Sci Technol*, 5 (2015) 807-817.
- [5] U. Hampel, R. Dittmeyer, A. Patyk, T. Wetzel, R. Lange, H. Freund, W. Schwieger, M. Grünwald, M. Schlüter, U. Petasch, The Helmholtz Energy Alliance "Energy Efficient Multiphase Chemical Processes", *Chem-Ing-Tech*, 85 (2013) 992-996.
- [6] A. Inayat, J. Schwerdtfeger, H. Freund, C. Körner, R.F. Singer, W. Schwieger, Periodic open-cell foams: Pressure drop measurements and modeling of an ideal tetrakaidecahedra packing, *Chem Eng Sci*, 66 (2011) 2758-2763.
- [7] M. Klumpp, A. Inayat, J. Schwerdtfeger, C. Körner, R.F. Singer, H. Freund, W. Schwieger, Periodic open cellular structures with ideal cubic cell geometry: Effect of porosity and cell orientation on pressure drop behavior, *Chem Eng J*, 242 (2014) 364-378.
- [8] E. Bianchi, W. Schwieger, H. Freund, Assessment of Periodic Open Cellular Structures for Enhanced Heat Conduction in Catalytic Fixed-Bed Reactors, *Adv Eng Mater*, in press, DOI 10.1002/adem.201500356.
- [9] D. Jacqmin, Calculation of Two-Phase Navier-Stokes Flows Using Phase-Field Modeling, *J Comput Phys*, 155 (1999) 96-127.
- [10] H. Ding, P.D.M. Spelt, C. Shu, Diffuse interface model for incompressible two-phase flows with large density ratios, *J Comput Phys*, 226 (2007) 2078-2095.
- [11] J. Kim, Phase-Field Models for Multi-Component Fluid Flows, *Commun Comput Phys*, 12 (2012) 613-661.
- [12] H. Abels, H. Garcke, G. Grün, Thermodynamically Consistent, Frame Indifferent Diffuse Interface Models for Incompressible Two-Phase Flows with Different Densities, *Math Mod Meth Appl S*, 22 (2012).
- [13] M. Ben Said, M. Selzer, B. Nestler, D. Braun, C. Greiner, H. Garcke, A Phase-Field Approach for Wetting Phenomena of Multiphase Droplets on Solid Surfaces, *Langmuir*, 30 (2014) 4033-4039.
- [14] D. Jacqmin, Contact-line dynamics of a diffuse fluid interface, *J Fluid Mech*, 402 (2000) 57-88.
- [15] P.T. Yue, J.J. Feng, Phase-field simulations of dynamic wetting of viscoelastic fluids, *J Non-Newton Fluid Mech*, 189 (2012) 8-13.
- [16] H. Marschall, X. Cai, M. Wörner, O. Deutschmann, Conservative finite volume discretization of the two-phase Navier-Stokes Cahn-Hilliard and Allen-Cahn equations on general grids with applications to dynamic wetting, (2016) in preparation.
- [17] X. Cai, H. Marschall, M. Wörner, O. Deutschmann, Numerical Simulation of Wetting Phenomena with a Phase-Field Method Using OpenFOAM®, *Chem Eng Technol*, 38 (2015) 1985-1992.
- [18] P.T. Yue, C.F. Zhou, J.J. Feng, Sharp-interface limit of the Cahn-Hilliard model for moving contact lines, *J Fluid Mech*, 645 (2010) 279-294.
- [19] W. Villanueva, G. Amberg, Some generic capillary-driven flows, *Int J Multiph Flow*, 32 (2006) 1072-1086.
- [20] H.G. Weller, G. Tabor, H. Jasak, C. Fureby, A tensorial approach to computational continuum mechanics using object-oriented techniques, *Comput Phys*, 12 (1998) 620-631.
- [21] X. Cai, M. Wörner, O. Deutschmann, Implementation of a Phase Field Method in OpenFOAM® for Simulation of Spreading Droplets and Verification by Test Problems, 7th Open Source CFD Int Conf (available online at

- <http://www.opensourcecfd.com/conference2013/proceedings-day-2>) Hamburg, Germany, 2013.
- [22] Q.I.E. Segers, Cutting bubbles using wire-mesh structures - direct numerical simulations, PhD thesis, Technische Universiteit Eindhoven, 2015.
- [23] R. Clift, J.R. Grace, M.E. Weber, Bubbles, drops, and particles, Academic Press, New York, 1978.
- [24] H. Ding, E.Q. Li, F.H. Zhang, Y. Sui, P.D.M. Spelt, S.T. Thoroddsen, Propagation of capillary waves and ejection of small droplets in rapid droplet spreading, J Fluid Mech, 697 (2012) 92-114.
- [25] P. Yue, J.J. Feng, Can diffuse-interface models quantitatively describe moving contact lines?, Eur Phys J Spec Top, 197 (2011) 37-46.
- [26] P.T. Yue, J.J. Feng, Wall energy relaxation in the Cahn-Hilliard model for moving contact lines, Phys Fluids, 23 (2011) 012106.
- [27] X.D. Wang, X.F. Peng, B.X. Wang, Contact angle hysteresis and hysteresis tension on rough solid surface, Chinese J Chem Eng, 12 (2004) 615-621.
- [28] M.W. Baltussen, Bubbles on the cutting edge : direct numerical simulations of gas-liquid-solid three-phase flows, PhD thesis, Technische Universiteit Eindhoven, 2015.

Figure captions

Fig. 1: 2D axisymmetric simulation of an air bubble rising in quiescent liquid.

Fig. 2: Influence of mesh resolution on bubble rise velocity.

Fig. 3: Influence of Cahn number on bubble rise velocity.

Fig. 4: Influence of Peclet number on bubble rise velocity. The dashed horizontal line denotes the experimental terminal bubble rise velocity.

Fig. 5: Terminal bubble Reynolds number as a function of the Eötvös number. Comparison of present numerical results with experimental data of Segers [22].

Fig. 6: Influence of mesh resolution on time evolution of gas-liquid interfacial area during the cylinder-induced bubble cutting process.

Fig. 7: Interface evolution during the bubble cutting process. (a) – (j): Experimental and numerical results from Segers [22] with t being reduced by 0.15 s in order to account for the smaller domain height in the present simulation. (k) – (o): Present simulation results ($\theta_c = 60^\circ$).

Fig. 8: Influence of cylinder wettability on the interface evolution during the bubble cutting process (top row $\theta_c = 30^\circ$, middle row $\theta_c = 60^\circ$, bottom row $\theta_c = 90^\circ$).

Fig. 9: Time evolution of bubble interfacial area during the cylinder-induced bubble cutting process for different cylinder wettability.

Fig. 10: Geometry of a representative part of the POCS considered in the present investigation with window size $s = 4 \text{ mm}$, strut diameter $d_s = 1 \text{ mm}$ and grid angle $\alpha = 90^\circ$. The whole structure is tilted by 45° .

Fig. 11: 3D perspective view of bubble rise through POCS of different wettability (left column $\theta_c = 0^\circ$, middle column $\theta_c = 90^\circ$, right column $\theta_c = 120^\circ$). The number in the lower right corner of each subfigure denotes time.

Fig. 12: 2D lateral view of bubble rise through POCS of different wettability (left column $\theta_c = 0^\circ$, middle column $\theta_c = 60^\circ$, right column $\theta_c = 90^\circ$). The number in the lower right corner of each subfigure denotes time.

Figures

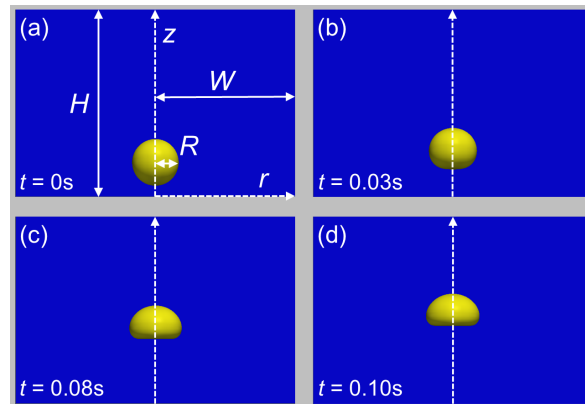


Fig. 1: 2D axisymmetric simulation of an air bubble rising in quiescent liquid.

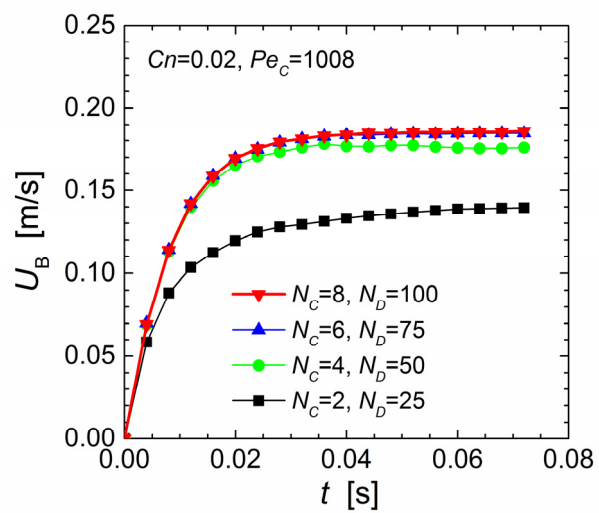


Fig. 2: Influence of mesh resolution on bubble rise velocity.

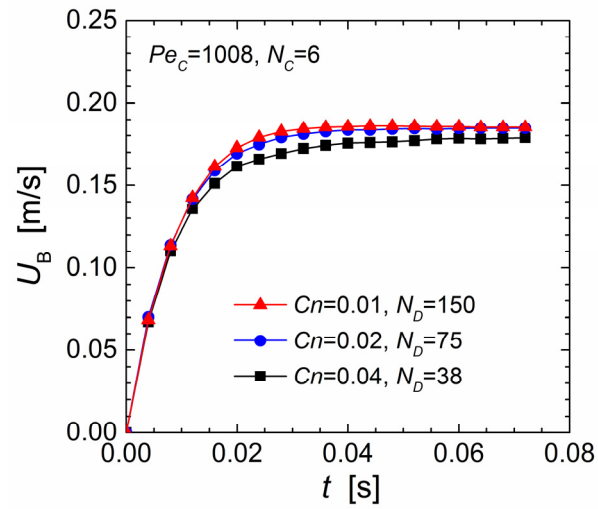


Fig. 3: Influence of Cahn number on bubble rise velocity.

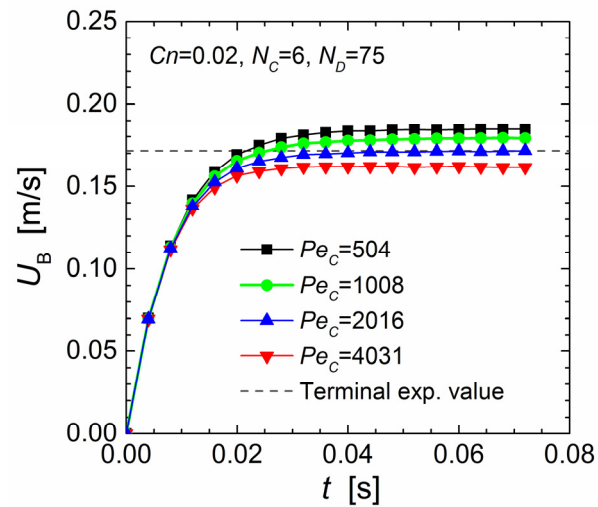


Fig. 4: Influence of Peclet number on bubble rise velocity. The dashed horizontal line denotes the experimental terminal bubble rise velocity.

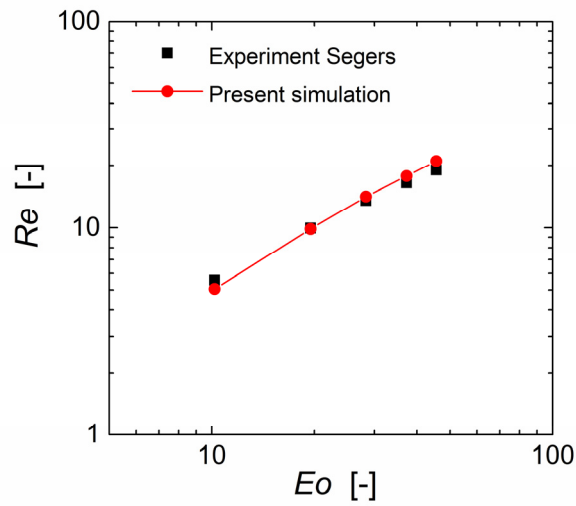


Fig. 5: Terminal bubble Reynolds number as a function of the Eötvös number. Comparison of present numerical results with experimental data of Segers [22].

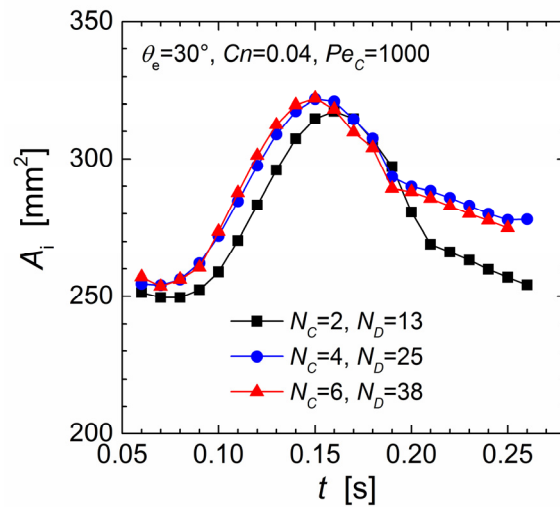


Fig. 6: Influence of mesh resolution on time evolution of gas-liquid interfacial area during the cylinder-induced bubble cutting process.

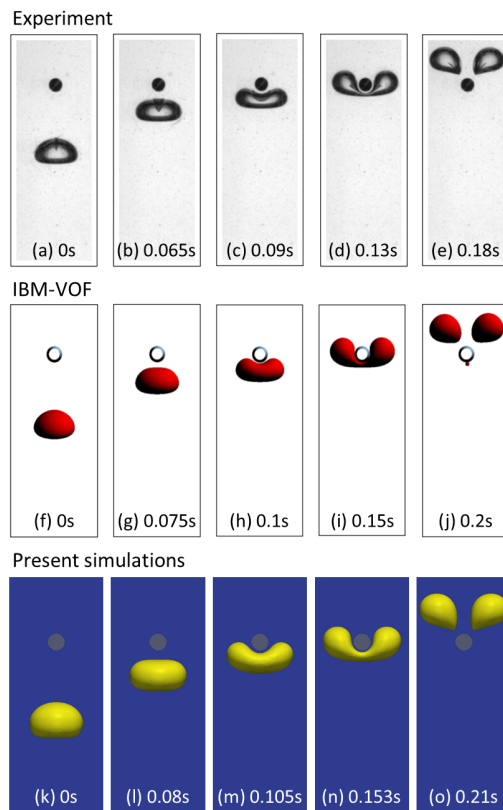


Fig. 7: Interface evolution during the bubble cutting process. (a) – (j): Experimental and numerical results from Segers [22] with t being reduced by 0.15 s in order to account for the smaller domain height in the present simulation. (k) – (o): Present simulation results ($\theta_e = 60^\circ$).

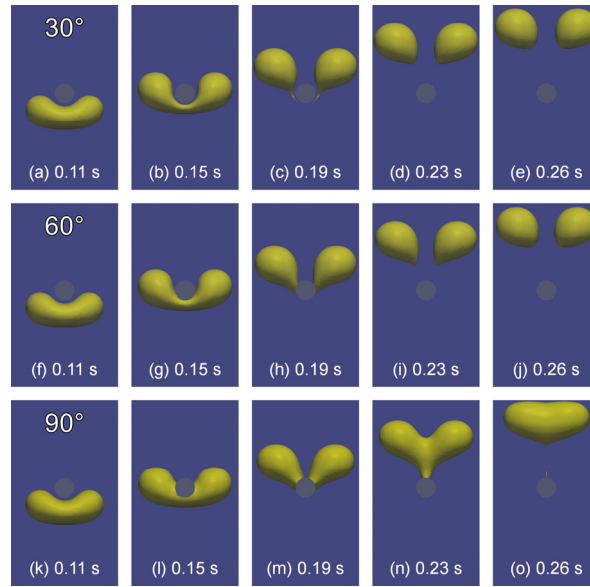


Fig. 8: Influence of cylinder wettability on the interface evolution during the bubble cutting process (top row $\theta_c = 30^\circ$, middle row $\theta_c = 60^\circ$, bottom row $\theta_c = 90^\circ$).

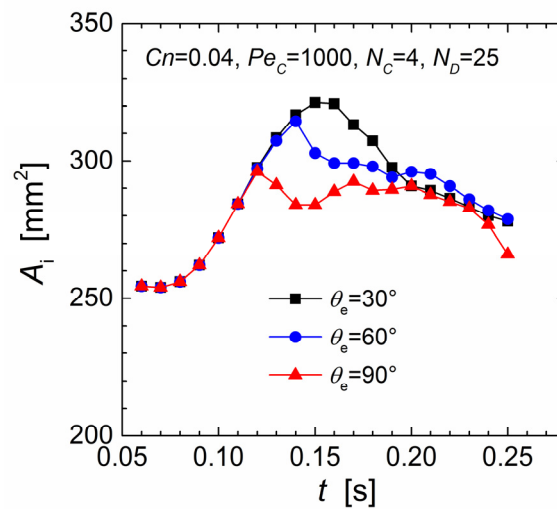


Fig. 9: Time evolution of bubble interfacial area during the cylinder-induced bubble cutting process for different cylinder wettability.

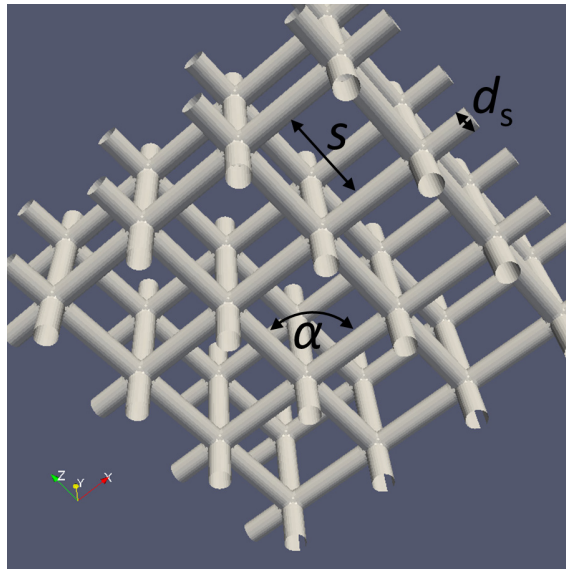


Fig. 10: Geometry of a representative part of the POCS considered in the present investigation with window size $s = 4 \text{ mm}$, strut diameter $d_s = 1 \text{ mm}$ and grid angle $\alpha = 90^\circ$. The whole structure is tilted by 45° .

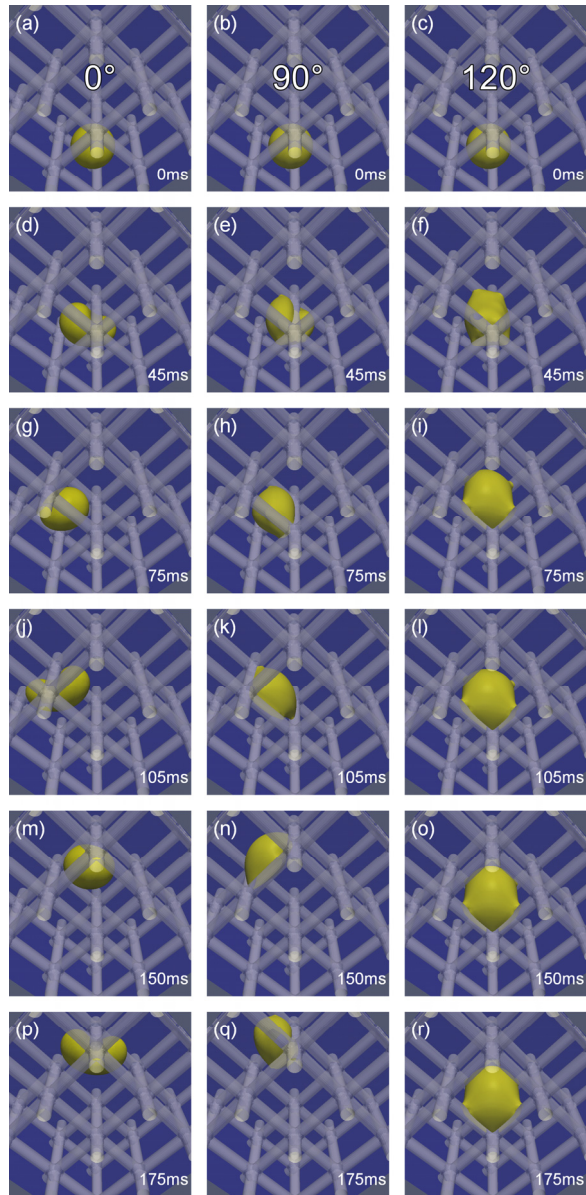


Fig. 11: 3D perspective view of bubble rise through POCS of different wettability (left column $\theta_c = 0^\circ$, middle column $\theta_c = 90^\circ$, right column $\theta_c = 120^\circ$). The number in the lower right corner of each subfigure denotes time.

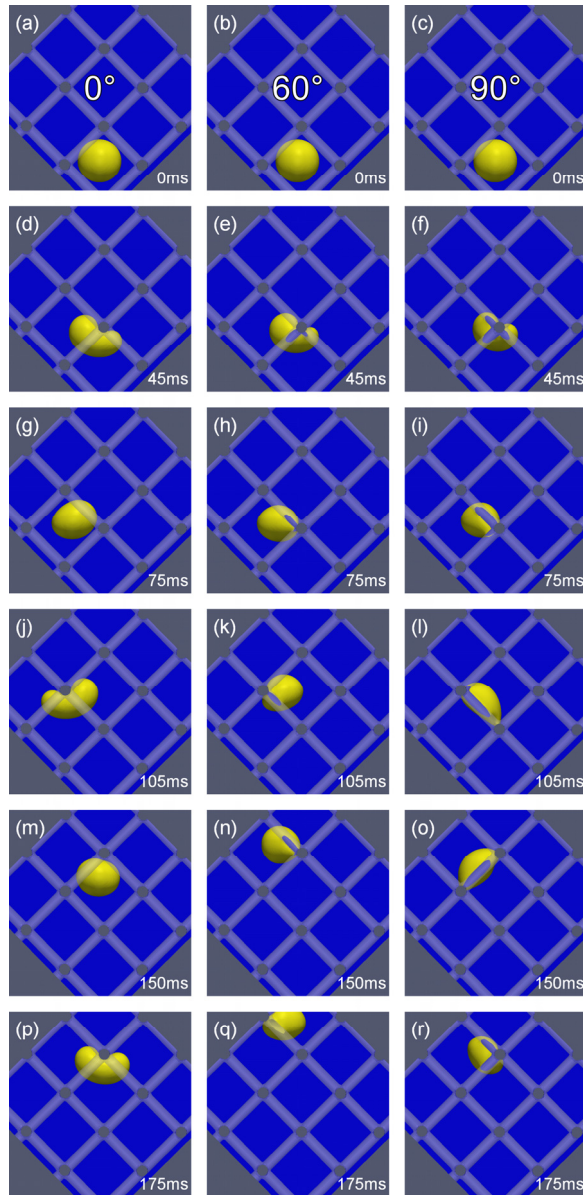
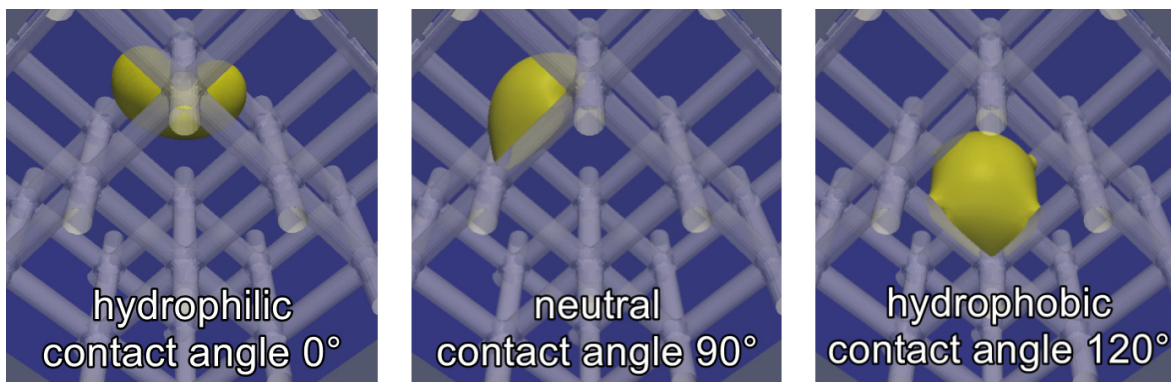


Fig. 12: 2D lateral view of bubble rise through POCS of different wettability (left column $\theta_c = 0^\circ$, middle column $\theta_c = 60^\circ$, right column $\theta_c = 90^\circ$). The number in the lower right corner of each subfigure denotes time.

Graphical abstract



Highlights

- Phase-field simulations of the buoyancy-driven rise of single bubbles
- Innovative numerical study for wettability dependent bubble-structure interaction
- Validation for instantaneous bubble cutting process by a horizontal solid cylinder
- Bubble rise through periodic open cellular structures of different wettability
- Hydrophilic structures appear beneficial for mass transfer and as catalytic support